Supplement of Atmos. Chem. Phys., 24, 23–40, 2024
https://doi.org/10.5194/acp-24-23-2024-supplement

Atmospheric Chemistry and Physics
Open Access
EGU

Supplement of

Tropospheric bromine monoxide vertical profiles retrieved across the Alaskan Arctic in springtime

Nathaniel Brockway et al.

Correspondence to: William R. Simpson (wrsimpson@alaska.edu)

HAIDI Instrument Details and DOAS Spectral Analysis

The HAIDI near-limb spectrometer recorded spectra with a resolution of roughly 0.55 nm FWHM in the range 301–408 nm. Three measurement spectra were coadded to reduce noise while maintaining good temporal resolution of 3 s for each observation. For the DOAS fit, reference spectra were often selected from the highest altitude portions of flights, generally around 1 km, with low SZAs. For the 26 flights with data from the forward spectrometer, 15 unique reference spectra were used. Low trace gas absorptions were confirmed for the reference spectra based on a pseudo-iterative approach to ensure that there were no drastically negative dSCDs.

Fit Range	331.8 - 369.6 nm
Reference Spectrum	Recorded near max flight altitude
Polynomial	3rd-order
Ring Spectra	Bussemer (1993), Quadratic Expansion
BrO	Fleischmann et al. (2004) 273K
NO_2	Bogumil et al. (2003) 243K
O_4	Thalman and Volkamer (2013) 253K
O_3	Serdyuchenko et al. (2014) 243K and 273K
OClO	Kromminga et al. (2003) 213K

Table S1. Fit parameters for the retrieval of BrO, NO_2, and O_4 dSCDs.

The fit parameters are shown in Table S1. The fit routine includes three Ring spectra, with a quadratic expansion, to account for rotational Raman scattering and its nonlinear impacts, using the methods from Bussemer (1993). The fit did not include HCHO, as it has a similar spectral structure to BrO, and fit uncertainties were reduced when it was not included. In testing, it was found not to have a large impact on the retrieved dSCDs, likely due to the remote location and clean atmosphere. Even in plumes downwind of Prudhoe Bay fossil fuel facilities, HCHO was not identified with confidence (i.e. dSCDs were below the detection limit). Further, final BrO dSCDs are lower in observations of these plumes, indicating that the omission of HCHO has little impact on BrO dSCDs, even in the few areas where we might expect HCHO. Synthetically adding HCHO absorption that corresponded to 200 pmol mol^{-1} to observed spectra resulted in a maximum BrO dSCD increase that was less than the 1σ fit error. Lastly, adding HCHO to the fit algorithm for the flight on April 1 resulted in almost entirely negative HCHO dSCDs and higher BrO dSCDs, though the increase was again less than the fit uncertainty. Therefore, the omission of HCHO possibly leads to an underestimation of BrO, but the uncertainty is less than many other sources of error.

The fit routine resulted in dSCDs for BrO, NO_2, and O_4 with detection limits of roughly 3.3×10^{13} molecules/cm^2, 2.8×10^{15} molecules/cm^2, and 1.4×10^{42} $molecules^2/cm^5$ based on median 2σ uncertainties. A typical dSCD retrieval is shown in Fig. S1. It should be noted that a newer O_4 cross-section has become available since spectra were originally fit (Finkenzeller and Volkamer, 2022). This cross-section was tested on one flight and had negligible impact on BrO and O_4 retrievals. However, this reference should be used in the future.

AMAX-DOAS Theory

A subset of data from a single porpoise is shown in Fig. S2 to display the different sensitivity each viewing angle has, with the observations from the four different viewing angles shown in the colored lines. The relative viewing angles are listed in the legend, however as the aircraft descends and ascends, the absolute viewing angle will change with the aircraft pitch angle. As the aircraft starts its descent with a mean pitch angle of -3.8°, all four observations show increasing BrO dSCDs, peaking near the bottom of this profile in the highest viewing angle, which is near-limb due to the negative pitch angle of the aircraft. However, as the aircraft ascends with a pitch angle of +4.7°, the lowest viewing angle is the nearest-limb observation resulting in that viewing angle observing the highest dSCDs. These observations indicate higher BrO concentrations toward the surface, however this is clearly a qualitative discussion. For quantitative results, we need to couple these observations to radiative transfer modelling.

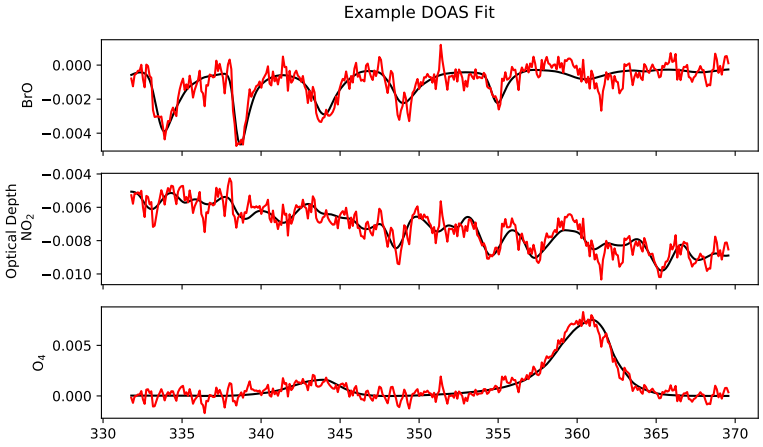

Figure S1. A typical dSCD fit result for BrO, NO_2, and O_4 with the absorption cross-section in black and the cross-section plus the fit residual in red. NO_2 and BrO fits result in negative coefficients, indicating more trace gas absorption in the measurement spectrum than the reference spectrum. Alternatively, there is less O_4 absorption in the measurement spectrum due to light cutoff by the surface, as this measurement was made at 140 m altitude and a viewing angle of $-1.85°$. Therefore, the "path length" is shorter in the observation spectrum compared to the reference. However, BrO and NO_2 are abundant enough at the surface to overcome this shorter path length, leading to positive absorption.

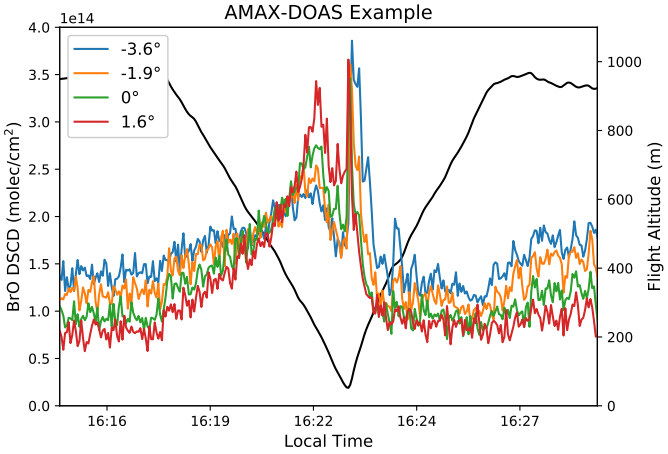

Figure S2. dSCD results from each viewing angle for an example atmospheric profile, where the listed viewing angles are relative to the aircraft. ALAR descended with a mean pitch angle of -3.8° in the left half of this figure, as seen by the altitude shown in black. During this time, the upward-most viewing angle (red) had the largest dSCD increase due to having the longest light path lengths through the lower atmosphere. Similarly, as the aircraft began to rise with a pitch angle of +4.7°, the largest dSCDs were observed in the lowest viewing angle for the same reason.

Radiative Transfer Model Initialization

Temperature and pressure were constrained with data from the aircraft for available flight altitudes for a given day. Temperatures above the maximum altitude were linearly interpolated to a 215 K tropopause located at 9 km. The temperature was then

held constant up to 29 km altitude before linearly increasing with altitude to 245 K at 48 km. The hypsometric approximation was used to calculate pressures above the maximum flight altitude.

A standard profile for ozone and NO_2 was scaled for each flight day based on the Ozone Monitoring Instrument total ozone column and tropospheric/total NO_2 column observations (Veefkind, 2012; Krotkov et al., 2019). The stratospheric BrO profile was determined from the Theys et al. (2009) climatology, based on the mean flight solar zenith angles, total ozone column, and stratospheric NO_2 column. Tropospheric BrO was set to 0.5 pmol mol^{-1} through the free troposphere, 1 pmol mol^{-1} between 500 and 700 m, 2.5 pmol mol^{-1} between 300 and 500 m, and 10 pmol mol^{-1} below 300 m. No diurnal variation was applied to the BrO profile, as flights were often near solar noon and lasted less than 4.5 hours. This BrO profile is also used as the apriori BrO profile for the BrO mixing ratio optimal estimation algorithm. Apart from these three trace gases, O_4 absorption and Rayleigh scattering are also included in VLIDORT calculations.

The particle loading was split into two particle types representing the upper atmosphere (above 6 km) and the lower atmosphere (below 6 km). The stratospheric particle loading was determined from the The Global Space-based Stratospheric Aerosol Climatology (Kovilakam et al., 2020) based on the measurement month and assuming a clean atmosphere. The aerosol particle extinction for the free troposphere was set to a constant 0.015 km^{-1}.

The particle extinction profile for the lower atmosphere was determined by first calculating a number density concentration from the Grimm particle counter (model 1.109) on ALAR (briefly described in Peterson et al. 2017) for each observation. This number density was then used to determine a mean particle profile shape from throughout each flight. The profile shape was then scaled to the total AOD from nearby Aeronet observations (Holben et al., 2001). This apriori particle extinction profile was then used as the input for the O_4 particle inversion to determine the final particle extinction profile of each flight. The Grimm only measures the particle size distribution (PSD) down to 0.25 μm. As the most optically relevant particles for UV-Vis remote sensing are smaller than 0.25 μm, we chose to use the number density as opposed to the surface area as the latter parameter would skew toward larger particles with less optical relevance to UV-Vis DOAS observations.

The optical properties for these two particle types were determined with a bulk Mie code, specifically designed for use with VLIDORT. The PSD for upper atmosphere particles was taken from Nyaku et al. (2020) based on their unimodal lognormal distribution fits and averaged over all altitude ranges. The refractive indices cited in Kovilakam and Deshler (2015) were also used here, with a wavelength-independent imaginary refractive index of 5×10^{-3}. Both the PSD and refractive indices of lower atmosphere particles were taken from Aeronet Version 3.0, Level 1.5 preliminary data (Sinyuk et al., 2020). Any missing data was set as the mean for the observation period. Considering that all particles considered were highly scattering and that the particle extinction inversion algorithm ensures the model matches observations, this preliminary data is likely not a significant source of uncertainty. The refractive indices and PSDs were then input to a bulk Mie code to produce aerosol scattering and extinction coefficients and moments. These results are used by VLIDORT to determine the angular scattering distribution as well as convert particle extinction between different wavelengths. Again, Grimm data was not used for the PSD input, as the instrument misses particles smaller than 0.25 μm.

VLIDORT operated at a wavelength of 350 nm for BrO and NO_2 observations (361 nm for O_4) and assumed a constant surface albedo of 0.825. This assumption could be incorrect for observations near sea ice leads. However, HAIDI forward-viewing observations show little impact on the intensity in the near-limb spectrometer when darker surfaces are underneath the aircraft. Although, this assumed albedo would need to be updated for nadir modelling. To save computational time, VLIDORT only simulated observations during the aircraft profiling of the atmosphere (Fig. 1), as well as several hand-selected areas of interest, resulting in roughly 60% of the observed spectra being modelled. For each simulation, a box air mass factor (BAMF) is calculated for each of the forward viewing angles, based on the aircraft pitch angle, aircraft altitude, and solar geometry.

Formally, the BAMF is defined as the partial derivative of the SCD with respect to the partial trace gas vertical column:

$$BAMF_i = \frac{\partial SCD}{\partial N_i} \tag{1}$$

where N is the partial vertical column density of the ith layer. The SCD can therefore by approximated by:

$$SCD = \sum_{i=1}^{n} BAMF_i \cdot C_i \cdot \Delta h_i \tag{2}$$

where Δh is the height of the ith grid cell and C is the trace gas concentration in that cell.

O_4 Inversion and Particle Extinction Profile Retrieval

Numerous techniques for solving the inverse problem to determine atmospheric parameters based on remote sensing observations are detailed in Rodgers (2000), and the specific method used here is based on the work of Baidar et al. (2013). The inversion technique relies on a forward model Jacobian matrix, such that

$$\boldsymbol{y} = \mathbf{K}\boldsymbol{x} + \varepsilon \tag{3}$$

where $\boldsymbol{y}$ is the measurement vector, $\boldsymbol{x}$ is the state vector we wish to retrieve, and ε is the combination of modelled and measured error. The forward model ($\mathbf{K}$) describes the sensitivity of the measurement vector to the state parameter, and takes the form:

$$\mathbf{K} = \frac{\partial \boldsymbol{y}}{\partial \boldsymbol{x}}. \tag{4}$$

However, there is a nonlinear relationship between the particle extinction profile and the observed O_4 SCD, thus necessitating an iterative approach.

O_4 DOAS observations can be used to inverse model particle extinction profiles, where the Jacobian matrix takes the form:

$$\mathbf{K} = \frac{\partial \boldsymbol{SCD_{O_4}}}{\partial \varepsilon_i}. \tag{5}$$

We can rearrange the Lambert-Beer law to define the SCD as:

$$SCD = \frac{1}{\sigma} \ln \frac{I_0}{I} \tag{6}$$

where I_0 is the intensity of light without the given absorber and σ is the absorption cross-section of the trace gas. By using this definition, we can calculate the Jacobian matrix as:

$$\mathbf{K} = \frac{1}{\sigma}\left(\frac{1}{I_0}\frac{\partial I_0}{\partial \varepsilon_i} - \frac{1}{I}\frac{\partial I}{\partial \varepsilon_i}\right) \tag{7}$$

where I_0 refers to a modelled radiance without O_4 absorption. The parameter $\frac{\partial I}{\partial \varepsilon_i}$ is the particle extinction Jacobian calculated by VLIDORT for a model run at 361 nm, which is in the middle of an O_4 absorption peak, with the model initialized as described in the previous section. This Jacobian describes how the particle extinction at each altitude impacts the modelled radiance at the observer both with (I) and without (I_0) O_4 absorption. As HAIDI retrieves dSCDs for each observation, we calculate the residual slant column density of the reference spectrum by running VLIDORT for the reference spectrum solar/measurement geometry to convert each observation to an SCD to use as the measurement vector ($\boldsymbol{y}$).

For the O_4 inversion, we utilized the Levenberg-Marquardt method (Levenberg, 1944; Marquardt, 1963), which is an iterative damped least-squares optimization where:

$$\boldsymbol{x_{i+1}} = \boldsymbol{x_i} + [(1+\gamma)\mathbf{S_a}^{-1} + \mathbf{K_i^T}\mathbf{S_\epsilon}^{-1}\mathbf{K_i}]^{-1}[\mathbf{K_i^T}\mathbf{S_\epsilon^{-1}}(\boldsymbol{y} - \hat{\boldsymbol{y}}) - \mathbf{S_a}^{-1}(\boldsymbol{x_i} - \boldsymbol{x_a})]. \tag{8}$$

This numeric solution is a function of the apriori particle extinction profile ($\boldsymbol{x_a}$), apriori error matrix ($\mathbf{S_a}$), the observations ($\boldsymbol{y}$), measurement error matrix ($\mathbf{S}_\epsilon$), and the modelled SCD ($\hat{\boldsymbol{y}}$) and Jacobian matrix ($\mathbf{K_i}$) calculated with the previous extinction profile (x_i). The apriori extinction profile is described above, and the uncertainty is set at 50% below 2 km and 2.5% above 2 km. This uncertainty profile ensures that the inversion will have a larger impact on the altitudes in which the observations are most sensitive. The diagonals of $\mathbf{S_a}$ are the squares of this uncertainty. The off-diagonal values are set at:

$$\mathbf{S}_{a_{ij}} = \sqrt{\mathbf{S}_{a_{ii}} \cdot \mathbf{S}_{a_{jj}} exp(-\ln(2) \cdot (\frac{Z_i - Z_j}{\delta})^2)} \tag{9}$$

where Z is the altitude grid and δ is a correlation length used to link nearby altitudes and smooth the resulting profile (described in Hendrick et al. 2004). In the O_4 inversion, a value of δ = 50 m is used.

The tuning parameter (γ) is used to increase the step size when the cost function is large and decrease the change in the retrieved profile as a minimum cost function is approached. We start with a γ of 0.01 and decrease by a factor of two if the cost function decreases and increase by a factor of 5 if the cost function increases. The cost function is defined as:

$$\chi^2 = (y - \hat{y})^T \mathbf{S}_{\delta\hat{\mathbf{y}}}^{-1} (y - \hat{y}) \tag{10}$$

where

$$\mathbf{S}_{\delta\hat{\mathbf{y}}} = \mathbf{S}_\epsilon (\hat{\mathbf{K}} \mathbf{S_a} \hat{\mathbf{K}}^{\mathbf{T}} + \mathbf{S}_\epsilon)^{-1} \mathbf{S}_\epsilon. \tag{11}$$

The algorithm is run at most eight times, though no run hit this threshold, until the cost function falls below 2x10^{90}, a number determined by trial and error. The cost function is so large because O_4 SCDs are typically on the order of 10^{43} molec^2/cm^5. More commonly, the algorithm stopped as the particle extinction profile no longer significantly changed between iterations, which occurred if the mean relative difference below 1 km altitude between the current and prior extinction profiles was less than 10%.

To determine the impact of the a priori profile on the retrieved particle extinction, data from the lofted BrO day on March 19 were reanalyzed with the a priori profile halved and doubled. In both cases, the root mean square difference below 1.5 km altitude between the resulting extinction profiles and the profile used in this work was roughly 0.04 km^{-1} with a mean absolute difference of 34%. This is comparable to the mean relative uncertainty of 27% retrieved by the optimal estimation. The a priori used on this day had a maximum extinction at the surface, but each of the three retrievals resulted in the maximum extinction being located above the surface with good correlation to the originally retrieved profile (mean R2 of 0.76).

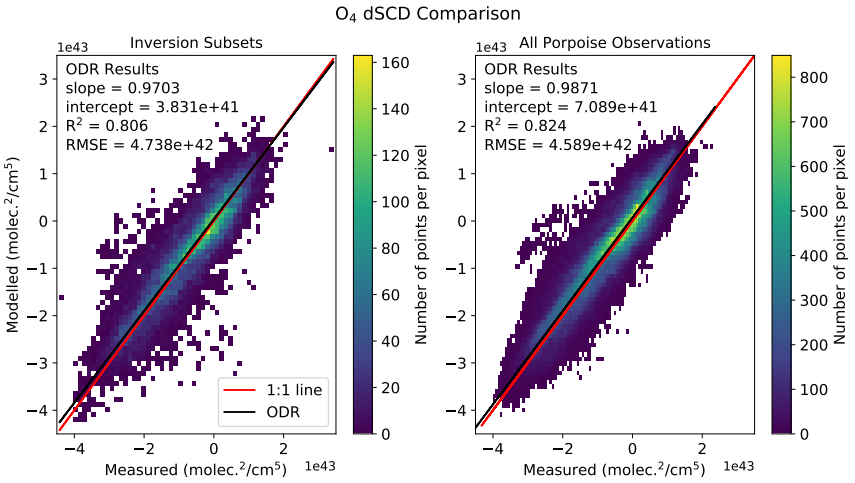

Figure S3. Comparison of modelled and observed O_4 dSCDs. The left plot shows results from all training subsets (800 points per flight) where the density plot shows most points lie along the 1:1 line. The black line indicates the results of an orthogonal distance regression on the two datasets, with a slope of 0.97. On the right, similarly good agreement is observed between measured and modelled dSCDs for all porpoise observations. In this case, the modelled dSCD is calculated with the 350 nm BAMF, the temperature and pressure profile, and a linear fit correction between 350 and 361 nm based on the training data.

This inversion algorithm results in modelled O_4 dSCDs that well-represent the observations. This is clear when comparing modelled and observed dSCDs for the training subsets (Fig. S3 left), where the modelled dSCDs fit the measured dSCDs with a RMSE of 4.74×10^{42} molecules/cm^2 and a R^2 of 0.806.

To determine how well the retrieved particle extinction profile agrees with all other measured O_4 dSCDs, modelled BAMFs were combined with apriori temperature and pressure profiles to model O_4 dSCDs. VLIDORT was constrained with the particle extinction profile retrieved from the O_4 inversion and run at 350 nm for all porpoise observations for use with BrO dSCDs.

The modelled O_4 dSCD from these BAMFs is thus for 350 nm, whereas the model was trained on calculations at 361 nm. To convert the modelled 350 nm dSCDs to 361 nm, the 350 nm dSCDs were fit against the 800 point training set calculated at 361. Results from an orthogonal distance regression were then used to convert all 350 nm dSCDs to 361 nm dSCDs. This is done for each flight individually, as each flight has a different pressure and temperature profile, particle extinction profile, and reference spectrum to offset modelled SCDs. The resulting comparison of the modelled 361 nm dSCD compared to HAIDI observations can be seen on the right side of Fig. S3. The agreement is very similar for all porpoise observations as it is for the training datasets, thus supporting the choice of using a single particle extinction profile for each flight.

BrO inversion

The combination of all BrO dSCD observations from each porpoise flight profile, down and up, were used for individual inversions to calculate BrO profiles (i.e. one BrO profile for each porpoise), which is solved via:

$$x = [\mathbf{K^T S_\epsilon}^{-1}\mathbf{K} + \mathbf{S_a}^{-1}]^{-1}[\mathbf{K^T S_\epsilon}^{-1}\boldsymbol{y} + \mathbf{S_a}^{-1}\boldsymbol{x_a}] \tag{12}$$

where $\mathbf{K}$ now has the form:

$$\mathbf{K} = \frac{\partial \boldsymbol{SCD_{BrO}}}{\partial N_{BrOi}} = \mathbf{BAMF}_i \tag{13}$$

to retrieve the vertical profile of column BrO. The resulting profile is then simply divided by the height of each grid cell to obtain a concentration profile. Again, we chose to use the SCD as the measurement vector by adding a modelled SCD_0, determined by running VLIDORT for the reference spectrum solar/measurement geometry, to the observed dSCDs.

The apriori error matrix is often used as a tuning parameter, and we vary the value based on measurement sensitivity to ensure that the inversion has the greatest impact on relevant altitudes. For altitudes in the range flown by the aircraft during a profile, the apriori uncertainty is 7.5 pmol mol^{-1}. For altitudes below this flight range that still show good measurement sensitivity (modelled BAMFs > 15), the uncertainty is set to 7.5 pmol mol^{-1}. If the modelled sensitivity is low, 2.5 pmol mol^{-1} is used. For altitudes above the flight range with good measurement sensitivity, the apriori uncertainty is 1 pmol mol^{-1}. For all other altitudes below 3 km, the uncertainty is also set to 0.25 pmol mol^{-1} and set to 0.05 pmol mol^{-1} above 3 km. This uncertainty profile ensures that the inversion has a larger impact on the altitudes with higher measurement sensitivity. Again, the off-diagonal values of this matrix are set as before, in this case with a correlation length of δ = 25 m.

BrO Error Propagation and Sensitivity Studies

It is important to properly quantify the uncertainty of the BrO profile retrievals, especially considering the many sources of uncertainty. The final uncertainty for BrO mixing ratio profiles comes from the root sum of square errors attributed to retrieval noise uncertainty, smoothing error, and forward model uncertainty. The retrieval noise arises from underlying measurement uncertainty.

The measurement uncertainty is the 1σ fit uncertainty of the BrO dSCDs with an additional 9% relative uncertainty due to cross-section error along with the uncertainty of the SCD_0 calculation. The uncertainty of the SCD_0 calculation derives from BAMF uncertainty (described below) and apriori profile uncertainty. For BrO, the SCD_0 was dominated by the stratosphere where the apriori uncertainty is due to the uncertainty of the stratospheric NO_2 columns used with the Theys et al. (2009) climatology as well as the impact of using a single stratospheric profile for an entire flight. The mean SZA of all measurements was 70°, with a maximum of 82.2°, and the average change in SZA throughout each flight was 6°. The impact of this SZA change on the BrO profiles was determined to be roughly 10% by applying the climatology with the maximum and minimum SZAs of each flight. This is considerably lower than the 33% uncertainty caused by NO_2 column uncertainty. Therefore, the stratospheric BrO apriori profile uncertainty was set at 33%. The final measurement uncertainty is then passed through the retrieval algorithm as described in Rodgers (2000).

The smoothing error is attributed to the fact that we cannot retrieve the true state of the retrieved parameter, but rather that parameter smoothed by the averaging kernel. Therefore, this uncertainty is based off of a combination of the apriori covariance

matrix and the averaging kernels. These two uncertainties were often comparable and range from 0–3 pmol mol^{-1} through the lower atmosphere.

To calculate the forward model uncertainty, we first must quantify the uncertainty of our BAMF calculations, which were largely due to assumptions made for radiative transfer modelling. Identified sources of error were: radiative transfer model linearization, surface albedo, measurement elevation angle, and particle extinction variability. First, a 5% model uncertainty was assumed. For the three other parameters, sensitivity tests were run by varying the values to determine the impact on BAMF calculations.

The albedo was assumed to be a constant 0.825 for all observations. Varying this parameter from 0.775 to 0.85 resulted in a 2% uncertainty that was largely unaffected by viewing geometry. Viewing angle uncertainty arises from the fact that the model is run for discrete viewing geometries, when light from a range of viewing angles enters the telescope (with a FWHM of 3.3°). The model was thus run for a range of of viewing angles, with resulting BAMFs averaged over the field of view (weighted with a Gaussian shape) and compared to BAMFs from a single view. This viewing angle uncertainty led to large BAMF uncertainty at flight altitude, where the impact was the largest. Lastly, a 50% uncertainty was used to vary the particle extinction profile to calculate the impact on BAMFs. The resulting uncertainty greatly depended on the viewing angle, with the largest impacts on the limb (20% uncertainty at flight altitude) and much lower impacts further away from the aircraft and at higher/lower angles (minimum of 4%). The final BAMF uncertainty thus depends on the flight altitude and viewing angle of each observation.

Due to the complex BAMF uncertainty, the ultimate forward model uncertainty was determined by applying the extreme uncertainty to the BAMFs and calculating the BrO profiles. The average impact was then used as the forward model uncertainty, which peaks at the surface due to a combination of the average particle extinction profile and path length truncation by the surface. This uncertainty dominates the BrO profile error at the surface, but is lower than the other two sources of uncertainty aloft.

Cluster Information

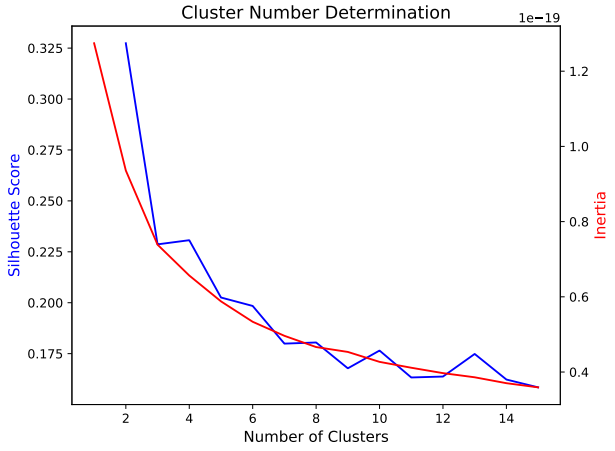

Figure S4. Results of the silhouette score test (blue) used to determine the number of clusters for the K-means analysis. We chose the second highest score of 4 clusters to get more detail about common profile shapes. The inertia (red) is also shown, although was not used to determine the number of clusters to include.

The choice of four BrO mixing ratio clusters was determined via the silhouette score (Fig. S4), which quantifies how much better a profile's cluster explains its shape compared to the next closest cluster. A higher silhouette score means that a certain number of clusters explains the shape of the profiles better than another number of clusters. In this case, two clusters had the

highest silhouette score. However, this provided us little additional information, as the profiles were grouped into a high and low BrO mixing ratio cluster. By using the number of clusters with the second highest silhouette score (4), we learned more information about common BrO profile shapes that still accounted for the total variability of the profiles well.

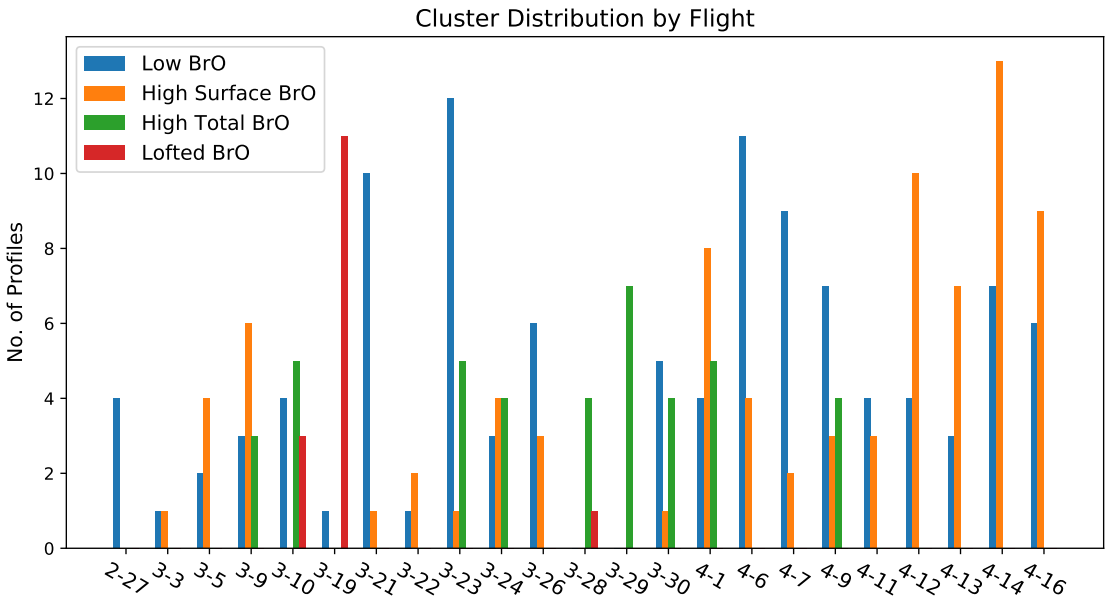

Figure S5. The distribution of each cluster as a function of flight. We saw no clear trend in the time of year that certain clusters were observed.

The total distribution of the four mixing ratio clusters may be of use to study the distribution of the different clusters and if there was any temporal trend. The total number of each clustered profile for each flight day is shown in Fig. S5 and Table S2. Low and high surface BrO clusters were seen throughout the campaign period, indicating that there was little temporal influence on the BrO profiles.

March 19, 2022 Lofted BrO Profiles

The majority (11 of 15) of the lofted BrO profiles were retrieved on a single day, March 19, 2022. This day was noted as being more hazy than other flight days. This can be seen in Fig. S6, which shows webcam images from HAIDI for two flight days. On the left is an image from March 19, 2022 where the haze is evident based on the lack of detail in the snow surface and the difficulty identifying the horizon. On the right side is a webcam image from a similar location and time of day on March 21, 2022. The visibility on this day was much better, as seen by the detail on the snow surface.

As the retrieved BrO profiles on this day greatly differ from most of the other retrieved profiles, it is important to confirm the retrieval. For this day, the larger particle extinction will decrease light paths through the lower atmosphere. The algorithm will thus result in larger mixing ratios from lower dSCDs. One simple option to verify the lofted BrO profiles is to investigate how the observed dSCDs change as a function of flight altitude. Figure S7 shows the dSCDs from the various porpoises on March 19 for two different viewing angles. The left side shows the descending portions of the porpoises along with the upward-most viewing angle, which results in a mean elevation angle of $-2.28°$. The right side of the figure shows the ascending portions along with the downward-most viewing angle, which results in a mean elevation angle of $+0.18°$. For both cases, we observed high dSCDs above the surface. This indicates that the shape of the underlying dSCD observations have a large impact on the retrieved mixing ratio profiles, and the lofted BrO cases are not due to auto-correlation with enhanced particle extinction.

Date	Low BrO #	High Surface BrO #	High Total BrO #	Lofted BrO #
2-27	4 (100%)	0 (0%)	0 (0%)	0 (0%)
3-3	1 (50%)	1 (50%)	0 (0%)	0 (0%)
3-5	2 (33%)	4 (67%)	0 (0%)	0 (0%)
3-9	3 (25%)	6 (50%)	3 (25%)	0 (0%)
3-10	4 (33%)	0 (0%)	5 (42%)	3 (25%)
3-19	1 (8%)	0 (0%)	0 (0%)	11 (92%)
3-21	10 (91%)	1 (9%)	0 (0%)	0 (0%)
3-22	1 (33%)	2 (67%)	0 (0%)	0 (0%)
3-23	13 (72%)	0 (0%)	5 (28%)	0 (0%)
3-24	3 (27%)	4 (36%)	4 (36%)	0 (0%)
3-26	6 (67%)	3 (33%)	0 (0%)	0 (0%)
3-28	0 (0%)	0 (0%)	4 (80%)	1 (20%)
3-29	0 (0%)	0 (0%)	7 (100%)	0 (0%)
3-30	5 (50%)	1 (10%)	4 (40%)	0 (0%)
4-1	4 (24%)	8 (47%)	5 (29%)	0 (0%)
4-6	12 (80%)	3 (20%)	0 (0%)	0 (0%)
4-7	9 (82%)	2 (18%)	0 (0%)	0 (0%)
4-9	8 (57%)	2 (14%)	4 (29%)	0 (0%)
4-11	4 (57%)	3 (43%)	0 (0%)	0 (0%)
4-12	4 (29%)	10 (71%)	0 (0%)	0 (0%)
4-13	3 (30%)	7 (70%)	0 (0%)	0 (0%)
4-14	7 (35%)	13 (65%)	0 (0%)	0 (0%)
4-16	6 (40%)	9 (60%)	0 (0%)	0 (0%)

Table S2. The total number of each BrO cluster retrieved is shown for each flight day. The percentage of each profile is listed for each day in parentheses.

Figure S6. Images from the forward viewing webcam on ALAR showing an example of the haze observed on March 19 (left) compared to a clear day (March 21, right). Both images were recorded in a similar location at a similar time of day.

The fact that Lofted BrO profiles were retrieved across the entire measurement area on March 19 indicates that this was a large scale event. To confirm this, Fig. S8 shows the maximum retrieved BrO vertical column for each pixel on March 19 from TROPOMI (via personal communication with Andreas Richter, Seo et al., 2019). This is preliminary data with a simplified air

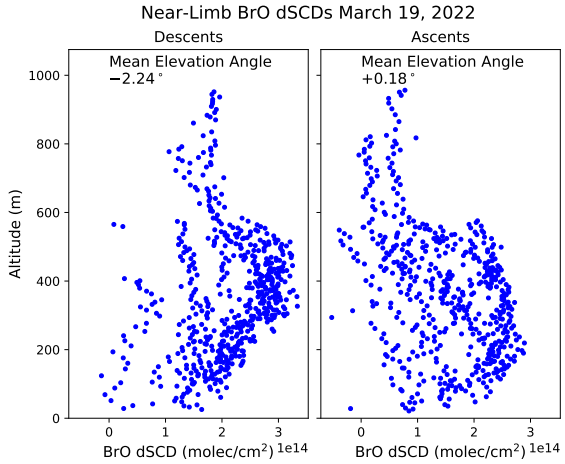

Figure S7. Retrieved near-limb dSCDs as a function of flight altitude for all porpoises on March 19. The left plot shows dSCDs from the upper-most viewing angle for all descending porpoise portions from the flight, resulting in a mean elevation angle of $-2.28°$. The right plot shows dSCDs from the lower-most viewing for all ascending portions of the porpoises, which results in a mean elevation angle of $+0.18°$. Both near-limb dSCD plots peak above the surface, supporting the retrieved Lofted BrO mixing ratio profiles on this day.

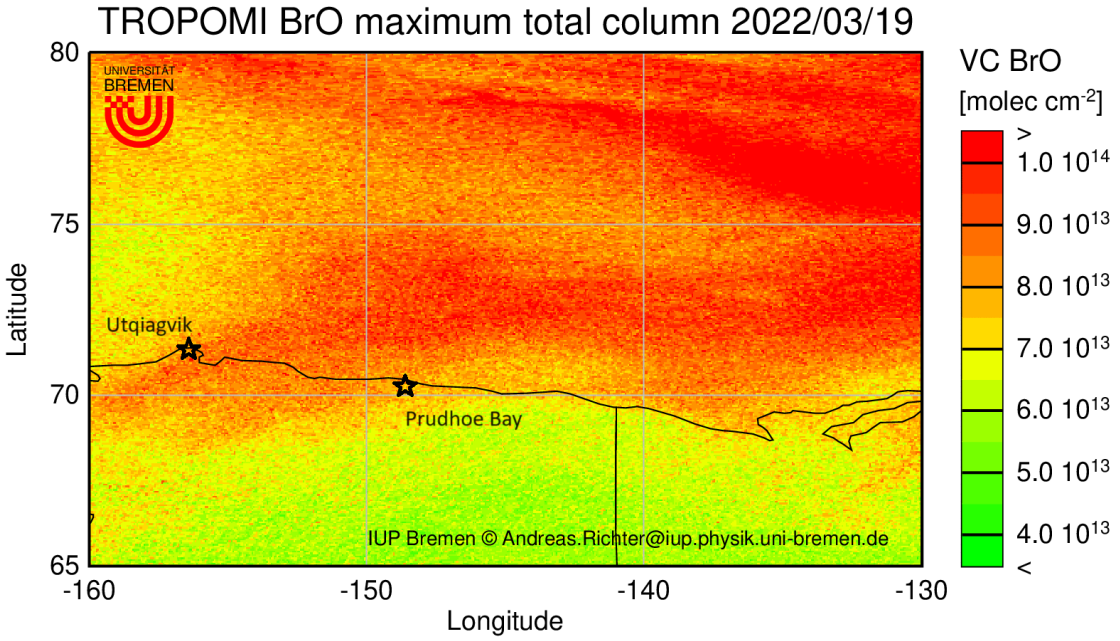

Figure S8. Maximum TROPOMI BrO vertical column density values (Seo et al., 2019) from March 19 confirm that this was a large-scale event. More work is needed to determine how observations from the satellite and HAIDI compare. This figure was provided via personal communication with Andreas Richter.

mass factor calculation and no cloud correction. However, this figure confirms the assertion of a large scale event. TROPOMI data confirms large BrO amounts throughout the measurement region, and indicates a connection to large BrO columns to the northeast.

Direct comparison of HAIDI observations to satellite data is difficult, as HAIDI observations are most sensitive to the lower atmosphere while satellite observations are most sensitive to the upper atmosphere. Therefore, considerable work is needed to compare column values from the two measurement techniques, which is beyond the focus of this work.

ALAR Average Parameters

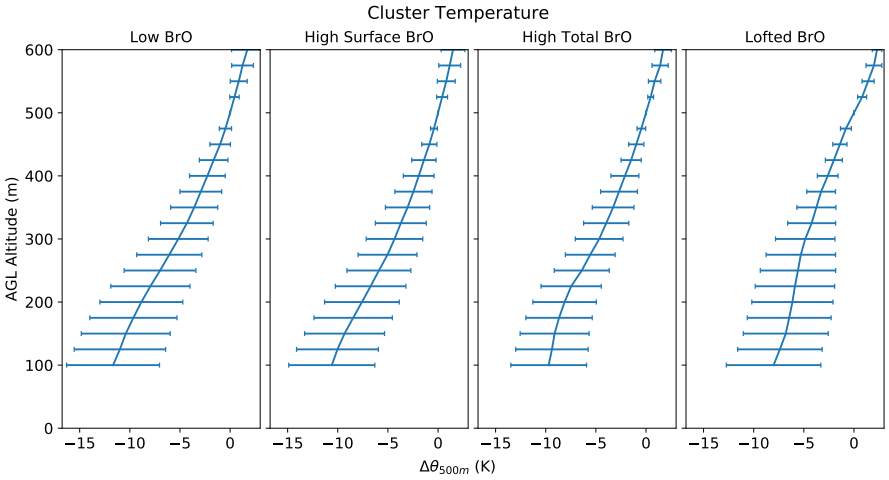

Figure S9. The standard deviation of the offset potential temperature shown in Fig. 10. The temperature at different levels is often not significantly different. However, we are more concerned with the shape of the different profiles, as this indicates the stability of the lower atmosphere.

For clarity, the data shown in Figs. 10 and 11 did not display the variability of the averaged parameters. These parameters are shown in this section (Figs. S9-S12) with their variability shown as error bars. The first parameter shown (Fig. S9) is the normalized potential temperature, which is the average potential temperature offset by the potential temperature at 500 m, hence why the variability at 500 m is zero. This variability shows that the four temperature profiles do not have significantly different temperatures at most altitudes. However, this parameter was used to discuss atmospheric thermodynamic stability, so we are much more interested in the lapse rate of the lower atmosphere than the total variability of these profiles.

Figure S12 shows the variability of the extinction profile for each cluster. As can be seen, the extinction profiles for the low BrO and high total BrO cases has significant variability at the surface. This large variability is due to the fact that the low BrO and high total BrO clusters were observed on March 23, 2022 where a particle extinction of 2.1 km^{-1} was retrieved at the surface. This was much higher than any other day (next highest was 0.65 km^{-1}).

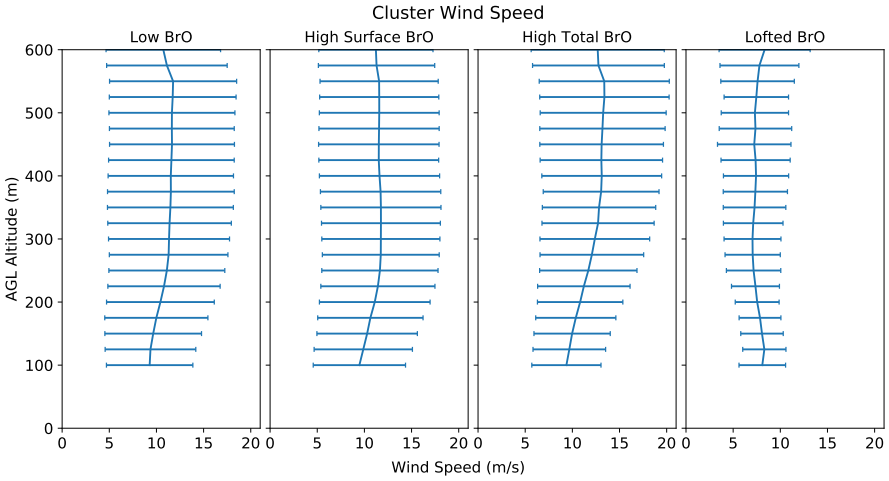

Figure S10. The standard deviation of the average cluster wind speed shown in Fig. 10.

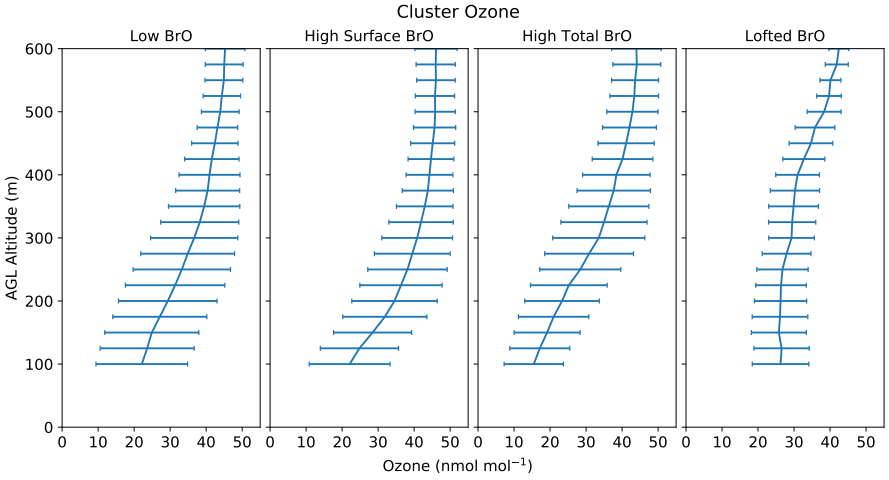

Figure S11. The standard deviation of the average ozone mixing ratio shown in Fig. 11.

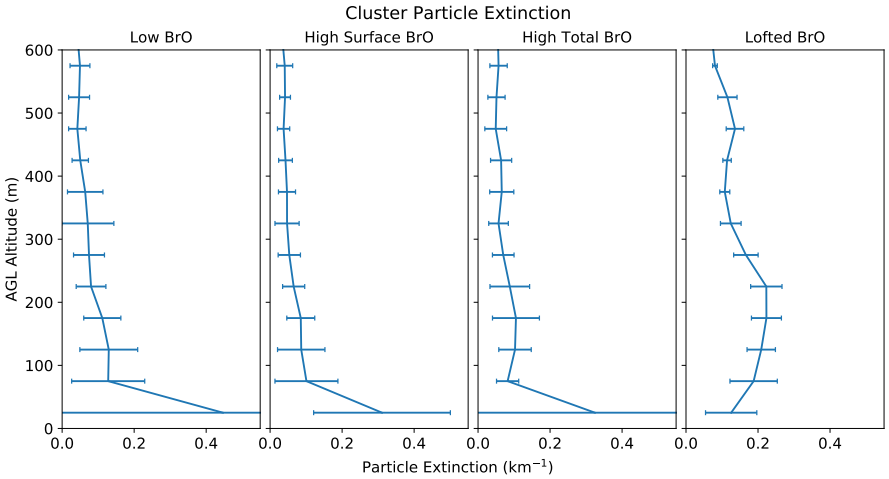

Figure S12. The standard deviation of the particle extinction profiles shown in Fig. 11. The variability at the surface for the low BrO and high total BrO cases is due to one day (March 23) with a much higher surface extinction than any other day (2 km^{-1} compared to 0.2 km^{-1} on average for all other days).

References

Baidar, S., Oetjen, H., Coburn, S., Dix, B., Ortega, I., Sinreich, R., and Volkamer, R.: The CU Airborne MAX-DOAS instrument: vertical profiling of aerosol extinction and trace gases, Atmos. Meas. Tech., 6, 719–739, https://doi.org/10.5194/amt-6-719-2013, 2013.

Bogumil, K., Orphal, J., Homann, T., Voigt, S., Spietz, P., Fleischmann, O. C., Vogel, A., Hartmann, M., Kromminga, H., Bovensmann, H., Frerick, J., and Burrows, J. P.: Measurements of molecular absorption spectra with the SCIAMACHY pre-flight model: Instrument characterization and reference data for atmospheric remote-sensing in the 230-2380 nm region, J. Photochem. Photobio. A, 157, 167–184, https://doi.org/10.1016/S1010-6030(03)00062-5, 2003.

Bussemer, M.: Der Ring-Effekt: Ursachen und Einfluß auf die spektroskopische Messung stratosphärischer Spurenstoffe, Diploma thesis, University of Heidelberg, 1993.

Finkenzeller, H. and Volkamer, R.: O2–O2 CIA in the gas phase: Cross-section of weak bands, and continuum absorption between 297–500 nm, J. Quant. Spectrosc. Radiat. Transfer, 279, 108 063, https://doi.org/https://doi.org/10.1016/j.jqsrt.2021.108063, 2022.

Fleischmann, O. C., Hartmann, M., Burrows, J. P., and Orphal, J.: New ultraviolet absorption cross-sections of BrO at atmospheric temperatures measured by time-windowing Fourier transform spectroscopy, J. Photochem. Photobio. A, 168, 117–132, https://doi.org/10.1016/j.jphotochem.2004.03.026, 2004.

Hendrick, F., Barret, B., Van Roozendael, M., Boesch, H., Butz, A., De Mazière, M., Goutail, F., Hermans, C., Lambert, J.-C., Pfeilsticker, K., and Pommereau, J.-P.: Retrieval of nitrogen dioxide stratospheric profiles from ground-based zenith-sky UV-visible observations: validation of the technique through correlative comparisons, Atmos. Chem. Phys., 4, 2091–2106, https://doi.org/10.5194/acp-4-2091-2004, 2004.

Holben, B. N., Tanré, D., Smirnov, A., Eck, T. F., Slutsker, I., Abuhassan, N., Newcomb, W. W., Schafer, J. S., Chatenet, B., Lavenu, F., Kaufman, Y. J., Castle, J. V., Setzer, A., Markham, B., Clark, D., Frouin, R., Halthore, R., Karneli, A., O'Neill, N. T., Pietras, C., Pinker, R. T., Voss, K., and Zibordi, G.: An emerging ground-based aerosol climatology: Aerosol optical depth from AERONET, J. Geophys. Res. Atmos., 106, 12 067–12 097, https://doi.org/https://doi.org/10.1029/2001JD900014, 2001.

Kovilakam, M. and Deshler, T.: On the accuracy of stratospheric aerosol extinction derived from in situ size distribution measurements and surface area density derived from remote SAGE II and HALOE extinction measurements, J. Geophys. Res. Atmos., 120, 8426–8447, https://doi.org/https://doi.org/10.1002/2015JD023303, 2015.

Kovilakam, M., Thomason, L. W., Ernest, N., Rieger, L., Bourassa, A., and Millán, L.: The Global Space-based Stratospheric Aerosol Climatology (version 2.0): 1979–2018, Earth Syst. Sci. Data, 12, 2607–2634, https://doi.org/10.5194/essd-12-2607-2020, 2020.

Kromminga, H., Orphal, J., Spietz, P., Voigt, S., and Burrows, J.: New measurements of OClO absorption cross-sections in the 325–435 nm region and their temperature dependence between 213 and 293 K, J. Photochem. Photobio. A, 157, 149–160, https://doi.org/https://doi.org/10.1016/S1010-6030(03)00071-6, 2003.

Krotkov, N. A., Lamsal, L. N., Marchenko, S. V., Celarier, E. A., J.Bucsela, E., Swartz, W. H., Joiner, J., and the OMI core team: OMI/Aura NO2 Total and Tropospheric Column Daily L2 Global Gridded 0.25 degree x 0.25 degree V3, https://doi.org/10.5067/Aura/OMI/DATA2018, 2019.

Levenberg, K.: A method for the solution of certain non-linear problems in least squares, Q. Appl. Math., 2, https://doi.org/10.1090/qam/10666, 1944.

Marquardt, D. W.: An Algorithm for Least-Squares Estimation of Nonlinear Parameters, J. Soc. Ind. Appl. Math., 11, https://doi.org/10.1137/0111030, 1963.

Nyaku, E., Loughman, R., Bhartia, P. K., Deshler, T., Chen, Z., and Colarco, P. R.: A comparison of lognormal and gamma size distributions for characterizing the stratospheric aerosol phase function from optical particle counter measurements, Atmos. Meas. Tech., 13, 1071–1087, https://doi.org/10.5194/amt-13-1071-2020, 2020.

Peterson, P. K., Pöhler, D., Sihler, H., Zielcke, J., General, S., Frieß, U., Platt, U., Simpson, W. R., Nghiem, S. V., Shepson, P. B., Stirm, B. H., Dhaniyala, S., Wagner, T., Caulton, D. R., Fuentes, J. D., and Pratt, K. A.: Observations of bromine monoxide transport in the Arctic sustained on aerosol particles, Atmos. Chem. Phys., 17, 7567–7579, https://doi.org/10.5194/acp-17-7567-2017, 2017.

Rodgers, C. D.: Inverse methods for atmospheric sounding: Theory and Practice, Series on Atmospheric, Oceanic and Planetary Physics–Vol. 2,, vol. 2, World Scientific Publishing, Singapore, 2000.

Seo, S., Richter, A., Blechschmidt, A.-M., Bougoudis, I., and Burrows, J. P.: First high-resolution BrO column retrievals from TROPOMI, Atmos. Meas. Tech., 12, 2913–2932, https://doi.org/10.5194/amt-12-2913-2019, 2019.

Serdyuchenko, A., Gorshelev, V., Weber, M., Chehade, W., and Burrows, J. P.: High spectral resolution ozone absorption cross-sections – Part 2: Temperature dependence, Atmos. Meas. Tech., 7, 625–636, https://doi.org/10.5194/amt-7-625-2014, 2014.

Sinyuk, A., Holben, B. N., Eck, T. F., Giles, D. M., Slutsker, I., Korkin, S., Schafer, J. S., Smirnov, A., Sorokin, M., and Lyapustin, A.: The AERONET Version 3 aerosol retrieval algorithm, associated uncertainties and comparisons to Version 2, Atmos. Meas. Tech., 13, 3375–3411, https://doi.org/10.5194/amt-13-3375-2020, 2020.

Thalman, R. and Volkamer, R.: Temperature dependent absorption cross-sections of O2-O2 collision pairs between 340 and 630 nm and at atmospherically relevant pressure., Phys. Chem. Chem. Phys., 15, 15 371–81, https://doi.org/10.1039/c3cp50968k, 2013.

Theys, N., Roozendael, M. V., Errera, Q., Hendrick, F., Daerden, F., Chabrillat, S., Dorf, M., Pfeilsticker, K., Rozanov, A., Lotz, W., Burrows, J. P., Lambert, J.-C., Goutail, F., Roscoe, H. K., and Mazière, M. D.: A global stratospheric bromine monoxide climatology based on the BASCOE chemical transport model, Atmos. Chem. Phys., 9, 831–848, https://doi.org/10.5194/acp-9-831-2009, 2009.

Veefkind, P.: OMI/Aura Ozone (O3) DOAS Total Column L3 1 day 0.25 degree x 0.25 degree V3, https://doi.org/10.5067/Aura/OMI/DATA3005, 2012.